

MORPHING TRAILING EDGE AERODYNAMICS AND THE ROLE OF TURBULENCE MODELING

P. Kovář[1, 2], J. Fürst[2], G. Frulla[3], G. M. Di Cicca[3] & E. Cestino[3]

[1]Center of Aviation and Space Research, Faculty of Mechanical Engineering, Czech Technical University, Jugoslávských partyzánů 1580/3, Prague, 16000, Czech Republic
[2]Department of Technical Mathematics, Faculty of Mechanical Engineering, Czech Technical University, Karlovo náměstí 13, Prague, 16000, Czech Republic
[3]Department of Mechanical and Aerospace Engineering, Polytechnic University of Turin, Corso Duca degli Abruzzi 24, 10129, Turin, Italy

Abstract

This paper investigates whether continuous morphing trailing edges provide measurable aerodynamic advantages over a conventional hinged aileron and, critically, whether such advantages can be identified reliably without flow-regime-consistent turbulence and transition modeling. A benchmark-driven computational framework is first established using the NACA0012, LS0417 (GA(W)-1), and FX66-S-196 V1 airfoils over fully turbulent and transitional Reynolds-number regimes. The validation stage shows that no single turbulence model is uniformly adequate across all cases: the preferred model depends on Reynolds number, boundary-layer state, and the presence of separation and transition. The reported results indicate that continuous morphing suppresses hinge-region loading discontinuities and improves peak aerodynamic efficiency by approximately 10-15% in representative cases, while wind-tunnel confinement produces non-negligible changes in both integrated aerodynamic coefficients and local pressure distributions. The results support morphing trailing edges as a promising aerodynamic control-surface concept and show that their assessment should be treated as a coupled problem of geometry, flow regime, and numerical-model fidelity.

Keywords: wing, morphing, CFD, turbulence modeling

1. Introduction

The present contribution demonstrates that the aerodynamic benefits of morphing trailing-edge concepts can be reliably identified and quantified only when turbulence and transition modeling are consistent with the actual flow regime. While morphing itself forms the core of this work, an important enabling contribution lies in showing that inappropriate turbulence modeling can fundamentally obscure or distort the true aerodynamic performance of the wing.

A comprehensive Computational Fluid Dynamics (CFD) validation campaign was conducted using three representative airfoils (NACA0012, LS0417, FX66-S-196 V1), spanning fully turbulent and transitional flow regimes over a wide range of Reynolds numbers. Systematic comparisons of multiple turbulence and transition models reveal that no single model is universally applicable, particularly in low Reynolds number flows and in regimes with laminar separation and transition. These findings are crucial for morphing aerodynamics, as unsuitable modeling may artificially delay separation, misrepresent pressure recovery, or mask efficiency gains attributable to morphing.

Building on this validated numerical foundation, the study presents detailed CFD-based comparisons between continuous morphing trailing edge concepts and a conventional aileron under identical aerodynamic conditions. Unlike classical ailerons, which inherently introduce hinge gaps, sharp curvature changes, and local pressure discontinuities, the investigated morphing concepts preserve surface

smoothness and camber continuity. This fundamental geometric advantage leads to smoother pressure distributions, reduced local suction peaks, and potentially lower structural and actuator loads.
One of the most significant outcomes is the observation that aerodynamic efficiency (lift to drag ratio) can be increased in optimal operating regions by tens of percent relative to an aileron-based configuration. These gains do not rely on large or aggressive deflections, but rather on subtle, continuous shape adaptation, clearly highlighting the inherent aerodynamic advantage and strong future potential of morphing control surfaces.
Additional investigations addressed wind-tunnel blockage effects using CFD, demonstrating that confinement has a non-negligible influence on both global aerodynamic coefficients and local pressure distributions. These effects were analyzed using a mesh overset strategy, which enables a flexible and numerically robust coupling between the airfoil grid and the surrounding wind-tunnel domain. Within the proposed simulation framework built on OpenFOAM [1], this approach allows efficient reconfiguration of tunnel geometry and blockage ratio without remeshing the airfoil itself, ensuring both numerical consistency and computational robustness across different test configurations. Accounting for blockage effects in this manner further improves the reliability of morphing performance assessment and strengthens the link between numerical predictions and experimental data.
The study proceeds in three stages. After the solver and turbulence models are tested and validated on the presented benchmarks. A cubic camber-line morphing parameterization is introduced and compared against a conventional 20% aileron on LS0417 at low Reynolds number. Furthermore, the influence of morphing start position is evaluated. Finally, a mesh overset wind tunnel framework is developed to assess blockage effects and to prepare for future experimental validation. Across a broad range of Reynolds numbers relevant to UAVs, light aircraft, and wind tunnel testing, morphing trailing edges exhibit stable and predictable aerodynamic behavior. This scalability underscores their suitability for applications ranging from low speed demonstrators to larger aircraft configurations.

2. Turbulence modeling and validation

All investigated applications correspond to low Mach number conditions, with $M < 0.3$, so the flow is treated as incompressible and solved within the OpenFOAM framework [1] using Semi-Implicit Method for Pressure Linked Equations (SIMPLE) algorithm [2].
Three benchmark airfoils as shown in Figure 1 are used. NACA0012 is employed as a high Reynolds number fully turbulent mesh validation case. LS0417 (GA(W)-1) is used both as a smooth profile benchmark and as the baseline airfoil for a 20% aileron and morphing trailing edge comparisons. FX66-S-196 V1 is used as a lower Reynolds number transition-sensitive benchmark. The benchmark campaign is used to determine which turbulence model family is appropriate in each flow regime before any morphing benefit is interpreted physically.

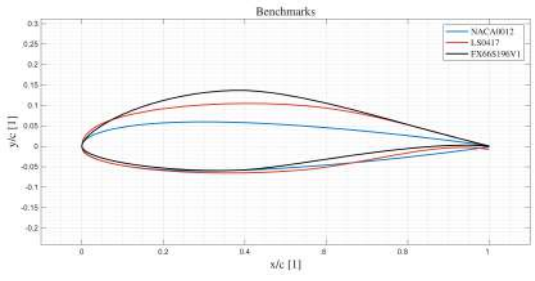


Figure 1 – Benchmark profiles comparison.

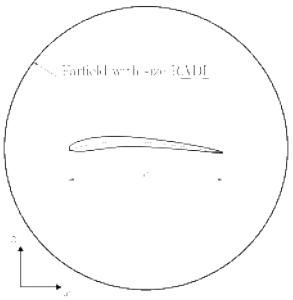


Figure 2 – Farfield mesh topology.

The same post-processing quantities are used throughout: lift coefficient C_l, drag coefficient C_d, pitching-moment coefficient at quarter chord $C_{m_{0.25c}}$, aerodynamic efficiency $E = C_l/C_d$, pressure coefficient C_p distribution, and skin-friction coefficient C_f distribution. The meshes are designed to keep dimensionless distance from the wall $Y^+ < 1$. Farfield topology is applied for the validation cases as it is shown in Figure 2 with a RADI parameter corresponding to one hundred unitary chords.

2.1 Fully turbulent case and effect of Reynolds number

Symmetrical profile NACA0012 was selected as the first and the simplest benchmark in order to identify suitable computational mesh resolution setup. According to literature [3, 4], the measurement was at Mach number $M = 0.15$ and Reynolds number $Re = 6 \times 10^6$. In combination with unitary chord length of the airfoil, it gives freestream velocity $U_\infty = 51.48 m s^{-1}$ and kinematic viscosity of the fluid $\nu = 8.58 \times 10^{-6} m^2 s^{-1}$. Reference values for force and moment coefficients estimation were assumed as $\rho_{ref} = 1 kg\, m^{-3}$, $p_{ref} = 0 Pa$, $U_{ref} = U_\infty = 51.48 m s^{-1}$. One equation Spalart-Allmaras turbulence model [5] was employed for the first benchmark as

$$\frac{\partial \nu_t}{\partial t} + \frac{\partial \nu_t u_j}{\partial x_j} = c_{b_1}(1 - f_{t_2}) S_t \nu_t - \left[c_{w_1} f_w - \frac{c_{b_1}}{\kappa^2} f_{t_2} \right] \left(\frac{\nu_t}{d} \right)^2 + \frac{1}{\sigma} \left[\frac{\partial}{\partial x_j} \left((\nu + \nu_t) \frac{\partial \nu_t}{\partial x_j} \right) + c_{b_2} \frac{\partial^2 \nu_t}{\partial x_i^2} \right]. \quad (1)$$

In Figure 3, there are comparisons of CFD results against experimental data provided by Gregory [3] in case of pressure coefficient distribution and a comparison against numerical data obtained by another CFD code presented by NASA [6] in case of friction coefficient.

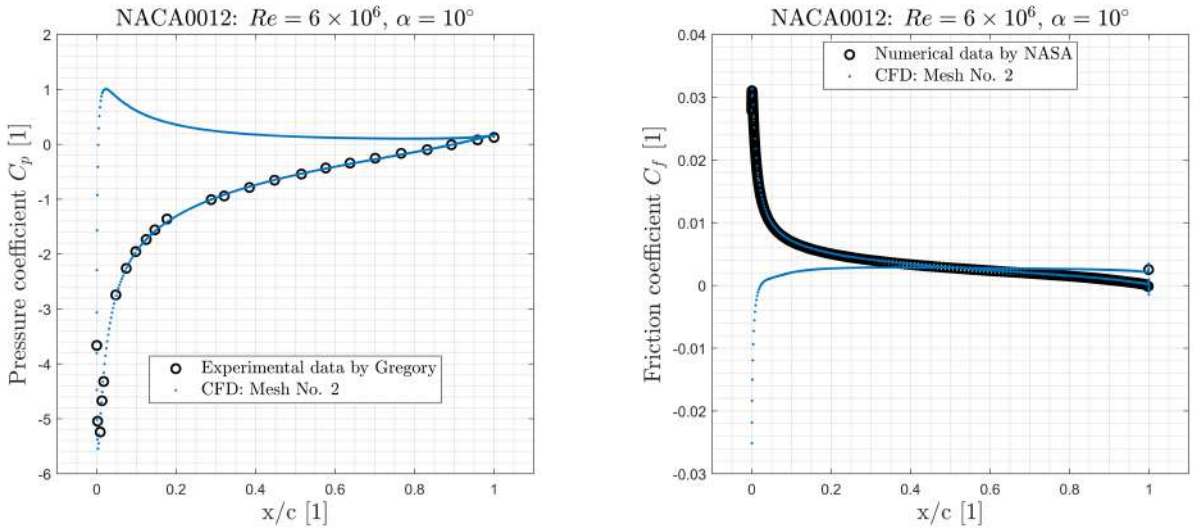


Figure 3 – NACA0012: Comparison of a pressure coefficient C_p and friction coefficient C_f distributions at Reynolds number $Re = 6 \times 10^6$ and angle of attack $\alpha = 10°$.

Resulting lift coefficient reached value $C_l = 1.277$ and the drag coefficient $C_d = 0.016$ under angle of attack $\alpha = 10°$ that correspond with data measured by Ladson [4] as shown in Figure 4.

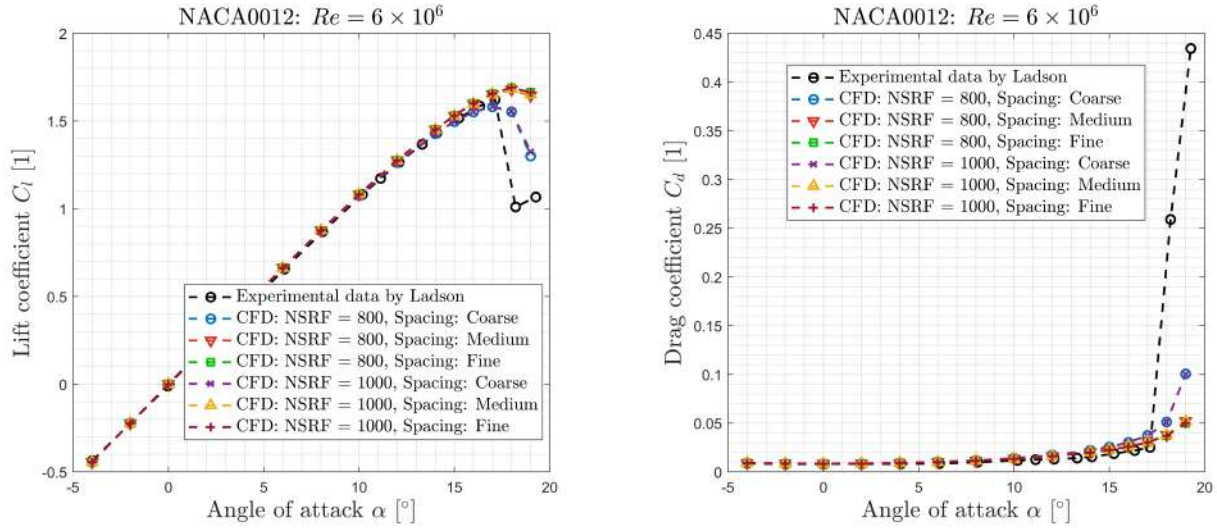


Figure 4 – NACA0012: Comparison of a lift coefficient C_l and drag coefficient C_d against angle of attack α at Reynolds number $Re = 6 \times 10^6$.

Initial airfoil that should be investigated more in detail is LS0417, also known as GA(W)-1, that was introduced by McGhee [7]. It is asymmetrical airfoil, which has maximum thickness 17% at 40% at the chord of profile that appears to be potentially suitable candidate to keep morphing structure inside. Experimental model was equipped with a strip of artificial roughness at the $x/c = 0.075$ of the chord as reported in [7, 8]. It means that natural transition should be avoided at higher Reynolds numbers, thus turbulence models that assume only fully developed flow should work properly. Turbulence models suitability was investigated, while computational mesh setup remained unchanged. Except for Spalar-Allmaras model, $k\omega$ models were employed. Standard $k\omega$SST model introduced by Menter [9] can be written as

$$\frac{\partial \rho k}{\partial t} + \frac{\partial \rho k U_j}{\partial x_j} = \tau_{ij}\frac{\partial U_i}{\partial x_j} - \beta^* \rho k \omega + \frac{\partial}{\partial x_j}\left[(\mu + \sigma^* \mu_t)\frac{\partial k}{\partial x_j}\right], \tag{2}$$

$$\frac{\partial \rho \omega}{\partial t} + \frac{\partial \rho \omega U_j}{\partial x_j} = \gamma \frac{\omega}{k}\tau_{ij}\frac{\partial U_i}{\partial x_j} - \beta^* \rho \omega^2 + \frac{\partial}{\partial x_j}\left[(\mu + \sigma \mu_t)\frac{\partial \omega}{\partial x_j}\right] - 2\rho(1-F_1)\sigma_2 \frac{1}{\omega}\frac{\partial k}{\partial x_j}\frac{\partial \omega}{\partial x_j}. \tag{3}$$

A modification of the $k\omega$SST with controlled decay, marked as $k\omega$SUST, should eliminate the non-physical decay of turbulence variables in the freestream conditions for external aerodynamic problems [10], through the addition of sustaining terms to the equations as

$$\frac{\partial \rho k}{\partial t} + \frac{\partial \rho k U_j}{\partial x_j} = \tau_{ij}\frac{\partial U_i}{\partial x_j} - \beta^* \rho k \omega + \frac{\partial}{\partial x_j}\left[(\mu + \sigma^* \mu_t)\frac{\partial k}{\partial x_j}\right] + \beta^* \rho k_{amb} \omega_{amb}, \tag{4}$$

$$\frac{\partial \rho \omega}{\partial t} + \frac{\partial \rho \omega U_j}{\partial x_j} = \gamma \frac{\omega}{k}\tau_{ij}\frac{\partial U_i}{\partial x_j} - \beta^* \rho \omega^2 + \frac{\partial}{\partial x_j}\left[(\mu + \sigma \mu_t)\frac{\partial \omega}{\partial x_j}\right] - 2\rho(1-F_1)\sigma_2 \frac{1}{\omega}\frac{\partial k}{\partial x_j}\frac{\partial \omega}{\partial x_j} + \beta^* \rho \omega_{amb}^2, \tag{5}$$

with the recommended farfield boundary conditions as

$$k_{farfield} = k_{amb} = 10^{-6} U_{ref}^2, \quad \omega_{farfield} = \omega_{amb} = \frac{5 U_{ref}}{L}. \tag{6}$$

Mach number during the experiment reported by McGhee was $M = 0.15$, that corresponds to the reference velocity $U_{ref} = 51.48 m s^{-1}$. Reference density and pressure was assumed as $\rho_{ref} = 1 kg m^{-3}$, $p_{ref} = 0 Pa$. Turbulence intensity and ratio of the viscosity to turbulent viscosity were assumed as $I = 1\%$ and $\nu/\nu_t = 0.1$, respectively, as boundary conditions for $k\omega$ turbulence models.
Courses of the lift coefficient C_l and pitching moment at the quarter of the chord $C_{m_{0.25c}}$, in Figure 5, are very similar in case of all turbulence models. Although $k\omega$ models should be more precise, simpler Spalart-Allmaras is closer to the experimental data provided by McGhee [7, 8, 11, 12], especially in the pitching moment coefficient, in case of higher Reynolds number.

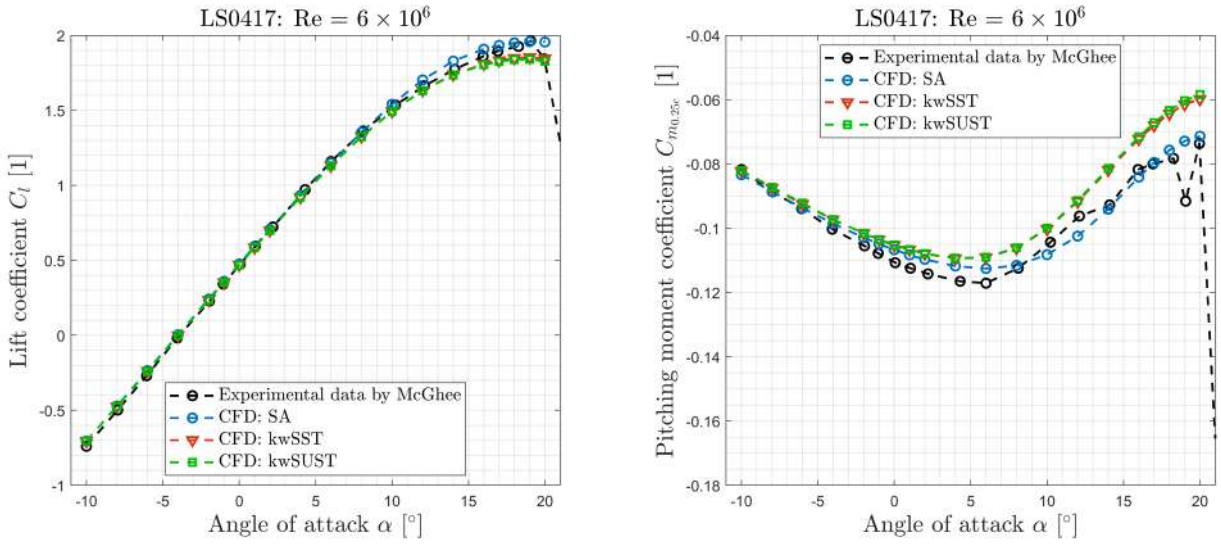


Figure 5 – LS0417: Comparison of a lift coefficient C_l and pitching moment at the quarter of the chord $C_{m_{0.25}}$ against angle of attack α at Reynolds number $Re = 6 \times 10^6$.

Another published flow regime is described by Reynolds number $Re = 2 \times 10^6$ and the same Mach number $M = 0.15$. Boundary conditions for turbulence quantities and reference values of density, and pressure remained as in the case of $Re = 6 \times 10^6$. As the Reynolds number decreased, kinematic viscosity ν was recalculated with respect to the unit chord of the airfoil for purposes of the simulation. The difference in the lift coefficient C_l, shown in Figure 6, can be seen especially at higher angles of attack. Although the pitching moment coefficient is captured similarly by presented turbulence models, Spalart-Allmaras model is outperformed by $k\omega$ models at lower Reynolds numbers.

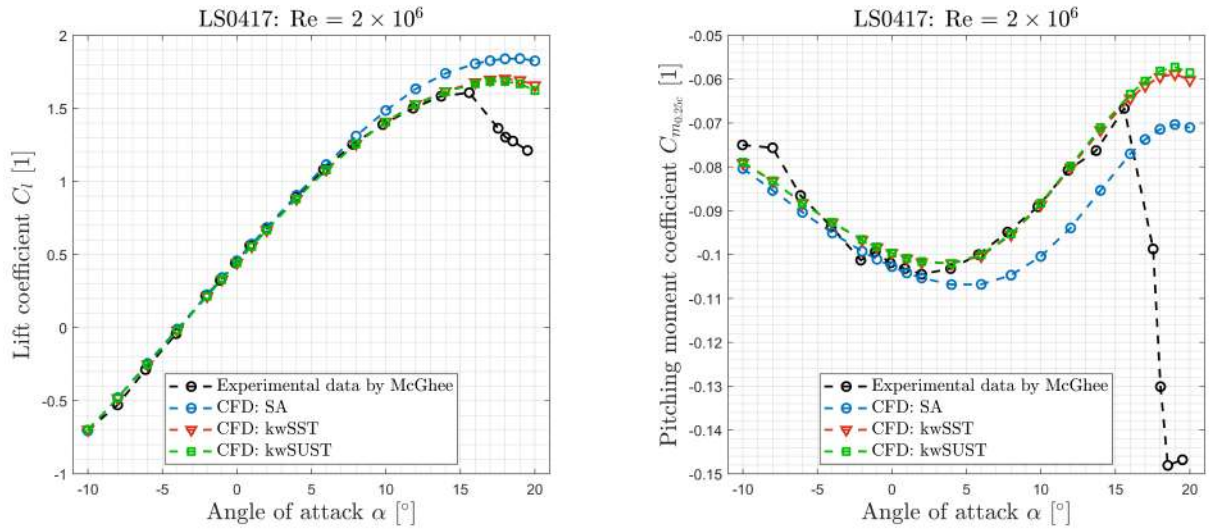


Figure 6 – LS0417: Comparison of a lift coefficient C_l and pitching moment at the quarter of the chord $C_{m_{0.25}}$ against angle of attack α at Reynolds number $Re = 2 \times 10^6$.

2.2 Fully turbulent case in the aileron configuration

Effects of classical aileron are investigated in further study. Experimental setup with the aileron and the axis of rotation located at $x/c = 0.8$ under Reynolds number $Re = 2.2 \times 10^6$ was reported in work of Wentz [13]. Bounds of the deflection were assumed as $\delta = \pm 10^\circ$ as it is indicated in Figure 7.

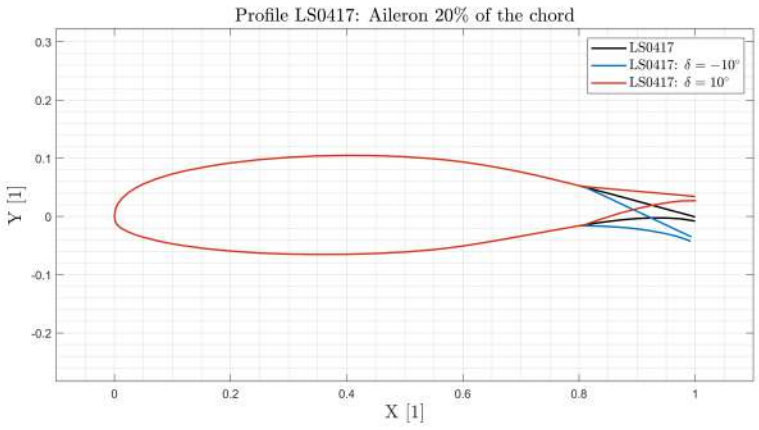


Figure 7 – LS0417 in the aileron configuration: Deflection bounds.

Measurements were performed at Reynolds number $Re = 2.2 \times 10^6$ and lower Mach number $M = 0.13$, that corresponds to the reference velocity $U_{ref} = 44.61 ms^{-1}$. For further study, farfield topology and $k\omega$SUST model was selected. Boundary conditions for turbulent quantities and reference values of density and pressure remained unchanged. Negative deflection δ refers to aileron downwards.
The pressure coefficient C_p distributions show that the CFD results reproduce the overall aerodynamic behavior of the LS0417 airfoil with good agreement compared to the experimental data of Wentz. In all cases, the numerical predictions capture the main suction peak near the leading edge and

the subsequent pressure recovery along the chord, indicating that the solver correctly predicts the dominant pressure loading on both suction and pressure surfaces as it can be seen in figures 8, 9.

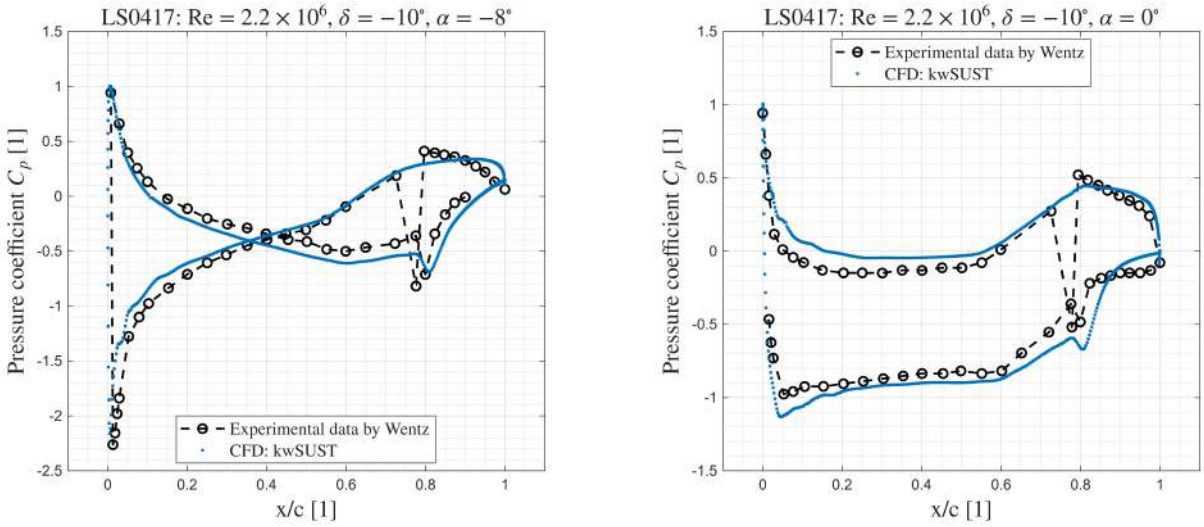


Figure 8 – LS0417 aileron configuration: Comparison of a pressure coefficient C_p distribution at $Re = 2.2 \times 10^6$ under negative and zero angles of attack $\alpha = \{-8; 0\}^\circ$ and $\delta = -10^\circ$ (downwards).

Particular attention should be given to the region around $x/c = 0.8$, where the aileron begins. Both the experimental and CFD results show a distinct change in the pressure distribution at this location, characterized by a local discontinuity or rapid variation in pressure coefficient C_p distribution. This behavior is associated with the hinge line and the change in local camber introduced by the aileron deflection. The CFD successfully captures this feature and follows the same trend observed experimentally, which is particularly important because this region strongly influences the control surface effectiveness and the resulting pitching moment.

For positive and negative aileron deflections, the pressure jump near $x/c = 0.8$ changes accordingly, reflecting the expected modification of the rear loading distribution. Negative deflection increases the pressure difference across the trailing edge region, while positive deflection reduces or reverses it, consistent with the physical effect of flap-like control surface motion. Although some local discrepancies in magnitude are observed, especially near the leading edge suction peak and in the immediate vicinity of the hinge point, the agreement in trend and pressure recovery demonstrates that the CFD model reliably predicts the aerodynamic response of the airfoil.

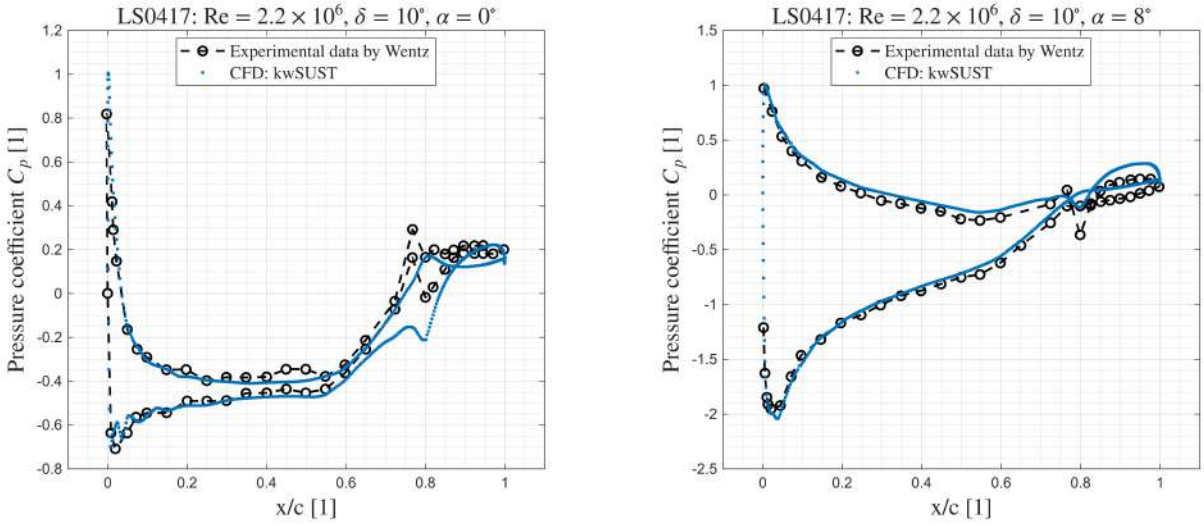


Figure 9 – LS0417 aileron configuration: Comparison of a pressure coefficient C_p distribution at $Re = 2.2 \times 10^6$ under zero and positive angles of attack $\alpha = \{0; 8\}^\circ$ and $\delta = 10^\circ$ (upwards).

Overall, the preservation of the same C_p trend, especially at the aileron onset location, confirms that the numerical model is capable of representing the pressure redistribution caused by aileron deflection and provides confidence in its use for further aerodynamic performance and control effectiveness analyses. The disturbances observed in the C_p distribution, particularly in the aileron hinge region around $x/c = 0.8$, have a direct influence on the integrated aerodynamic forces and therefore on the overall pitching moment coefficient $C_{m_{0.25c}}$ as it can be seen in Figure 10. Prediction matches experimental data at non-negative deflection angles. When the aileron is downwards, absolute value of the pitching moment is overestimated, especially at lower angles of attack.

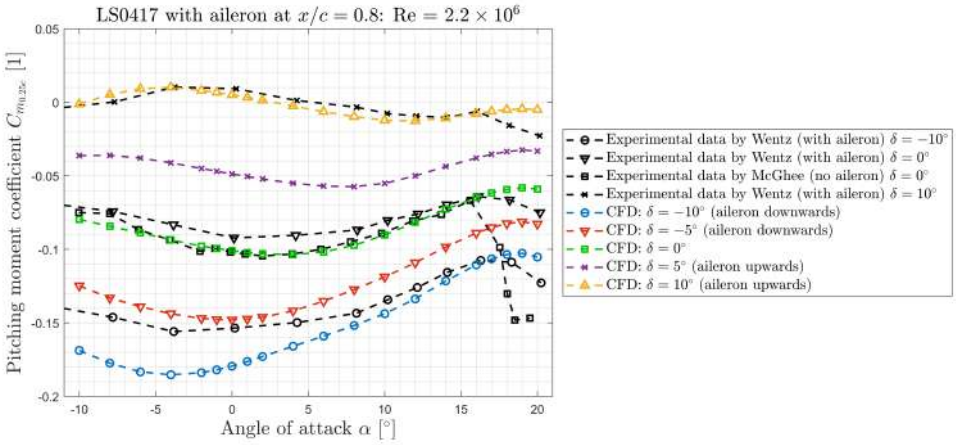


Figure 10 – LS0417, aileron configuration: Pitching moment coefficient $C_{m_{0.25c}}$ against angle of attack α at Reynolds number $Re = 2.2 \times 10^6$ under various deflection angles δ.

In the present results, the CFD results show a slight overestimation of lift compared to the experimental data by Wentz, which can be attributed to the stronger suction levels and smoother pressure recovery predicted numerically. This suggests that the numerical model slightly overpredicts the aerodynamic loading of the airfoil control surface system. In Figure 11, there is a comparison of the lift coefficient C_l against angle of attack α for different angles of the aileron deflection δ with experimental data provided by McGhee [8] and Wentz [13] for the case of smooth profile and case of the aileron.

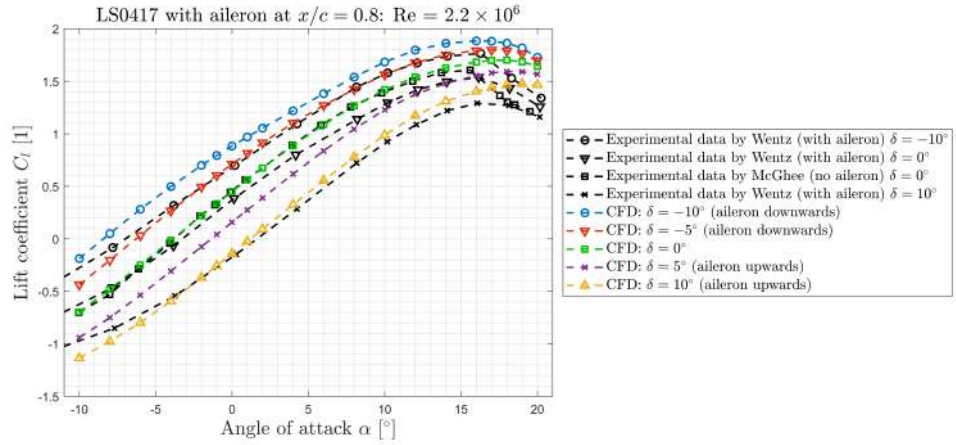


Figure 11 – LS0417, aileron configuration: Lift coefficient C_l against angle of attack α at Reynolds number $Re = 2.2 \times 10^6$ under various deflection angles δ.

It should be noted that for another a separate experimental campaign reported by McGhee, performed on the same LS0417 airfoil but with a smooth (non-hinged) configuration, the CFD predictions showed very good agreement with the measured integrated aerodynamic forces. This indicates that the observed discrepancies are likely linked to the increased sensitivity of the flow to local surface geometry, hinge-region disturbances, and experimental setup effects associated with the aileron configuration, rather than a fundamental limitation of the CFD approach itself.

2.3 Natural transition and fully turbulent assumption comparison

Unlike previous case of LS0417 profile and its experimental setup, in case of Wortmann's FX66-S-196-V1 [14] there is no strip with artificial roughness, thus, the flow is not fully turbulent and natural transition of the flow can occur. It was shown, that $k\omega$SUST turbulence model perform properly, when the flow is fully turbulent. Transition models γSUST that assumes flow intermittency and more advanced $\gamma\hat{R}e_{\theta t}$SUST [15, 16], both employed with controlled decay are added into the comparison. Additional transport equations of the γ and $\hat{R}e_{\theta t}$ [17] models can be written as follows

$$\frac{\partial \rho\gamma}{\partial t}+\frac{\partial \rho\gamma U_j}{\partial x_j}=P_\gamma-E_\gamma+\frac{\partial}{\partial x_j}\left[\left(\mu+\frac{\mu_t}{\sigma_f}\right)\frac{\partial\gamma}{\partial x_j}\right], \tag{7}$$

$$\frac{\partial \rho\hat{R}e_{\theta t}}{\partial t}+\frac{\partial \rho\hat{R}e_{\theta t}U_j}{\partial x_j}=P_{\theta t}+\left[(\mu+\mu_t)\frac{\partial\hat{R}e_{\theta t}}{\partial x_j}\right]. \tag{8}$$

The difference between mentioned transition models is that γSUST models does not deal with the second equation for $\hat{R}e_{\theta t}$. Inlet boundary conditions for the models are, according to [18],

$$\gamma=1, \tag{9}$$

$$\hat{R}e_{\theta t}=\begin{cases}1173.51-589.428I+\dfrac{0.2196}{I^2} & \text{if} \quad I\leq 1.3\% \\ \dfrac{331.5}{(I-0.5659)^{0.671}} & \text{if} \quad I>1.3\%,\end{cases} \tag{10}$$

where symbol I stands for the turbulence intensity at the inlet. On the wall, there is prescribed zero gradient for the γ and $\hat{R}e_{\theta t}$. Viscosity ratio is prescribed as 0.1 and turbulence intensity as 1%.
Validation of the transition turbulence models starts from the highest Reynolds number presented by Gooden [19], *i.e.*, Reynolds number $Re=2\times10^6$. It corresponds to reference velocity $U_{ref}=30ms^{-1}$, when kinematic viscosity of the air $\nu=1.5\times10^{-5}m^2s^{-1}$ and unit chord length are taken into account. Reference density and pressure was assumed as $\rho_{ref}=1kgm^{-3}$, $p_{ref}=0Pa$ as in previous cases.
In case of the lift and the drag in Figure 12, it can be seen that coefficients are captured more accurately by transition models in comparison with the fully turbulent model $k\omega$SUST.

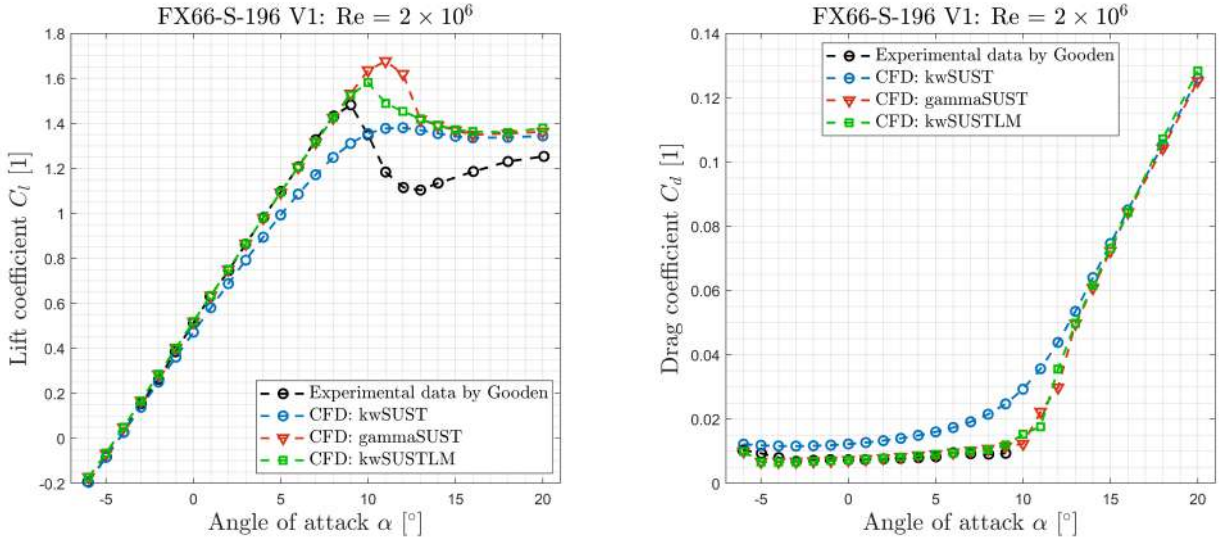


Figure 12 – FX66-S-196 V1: Comparison of a lift coefficient C_l and drag coefficient C_d against angle of attack α at Reynolds number $Re=2\times10^6$.

The last presented case is at Reynolds number $Re=0.5\times10^6$. According to previous considerations, reference velocity is $U_{ref}=7.5ms^{-1}$ in this case. Gooden [19] reported pressure coefficient distribution C_p under zero incidence angle $\alpha=0°$. Laminar separation bubble effect should be captured using this pressure distribution. Skin friction coefficient C_f distribution is also presented for the better visibility of such complex phenomenon as separation, transition and reattachment of the flow.

Separation of the flow can be observed on both sides of the airfoil. Its beginning is approximately at 50% of the chord and the reattachement approximately at 57% as reports Figure 13. It is captured also in the skin friction coefficient. It can be observed that the $k\omega$SUST turbulence model lacks the ability to capture natural transition phenomena. Moreover, unlike more advanced models such as γSUST or $\gamma\hat{R}e_{\theta t}$SUST, it does not predict any flow separation according to the friction coefficient.

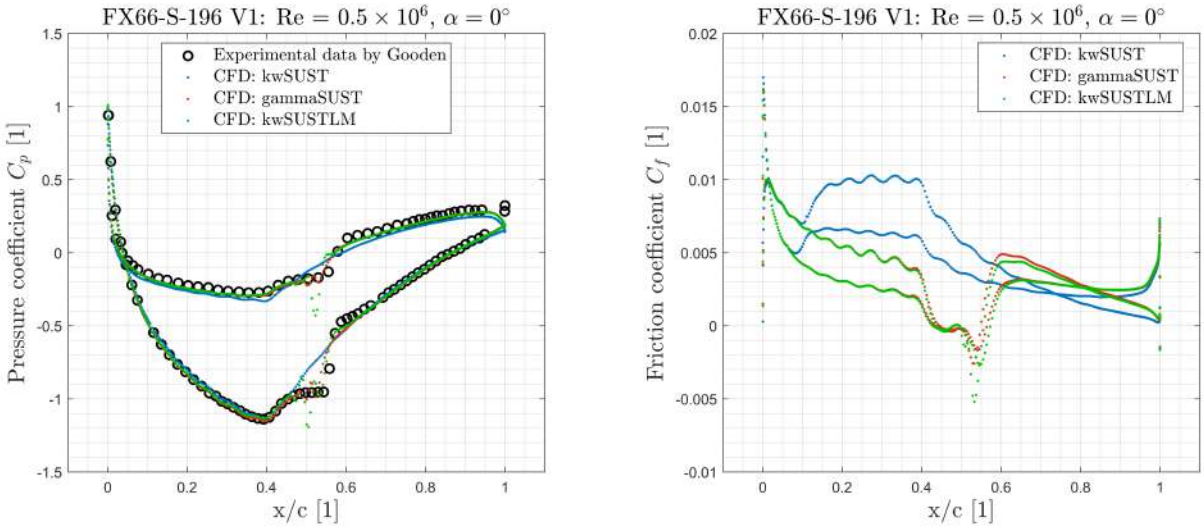


Figure 13 – FX66-S-196 V1: Comparison of a pressure coefficient C_p and friction coefficient C_f distributions at Reynolds number $Re = 0.5 \times 10^6$ and zero angle of attack $\alpha = 0°$.

It can be seen that these discrepancies at higher angles of attack result into larger differences in lift and drag coefficients in this case compared to higher Reynolds number case as showing Figure 14. It should be mentioned, that when there is no turbulizer in the experimental setup, standard turbulence models without transition are inappropriate for the simulation, especially at lower Reynolds number.

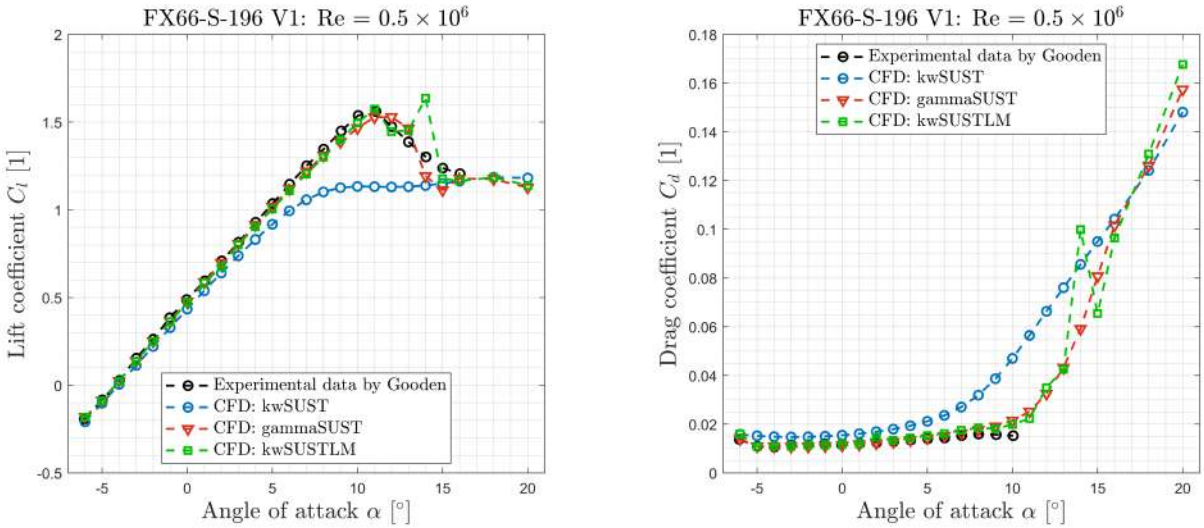


Figure 14 – FX66-S-196 V1: Comparison of a lift coefficient C_l and drag coefficient C_d against angle of attack α at Reynolds number $Re = 0.5 \times 10^6$.

3. Results

The case study is performed as the representative of the possible experimental assessment. According to wind tunnel measurement space, the profile chord $c = 250mm$ was selected. Together with reference velocity $U_{ref} = 50ms^{-1}$ and kinematic viscosity of the air $\nu = 1.5 \times 10^{-5}m^2\,s^{-1}$, it results into Reynolds number $Re = 0.833 \times 10^6$. An artificial roughness near the leading edge is assumed, thus, $k\omega$ models were chosen and turbulent boundary conditions remained unchanged.

3.1 Effect of the morphing at freestream

Morphing strategy is based on the camber line modification using cubic polynomial function. It means, that there are four unknown parameters $\{a_0, a_1, a_2, a_3\}$ which defines the cubic, thus, four constraints have to be prescribed. When the starting point of the morphing section is selected, three conditions are set herein - smooth and continuous derivatives up to the second order, that ensures $\mathscr{C}^2$ continuous transition. There is the last parameter to set at the end, that is angle of the trailing edge deflection δ. Unknown parameters are obtained by solving of a linear system as

$$\begin{pmatrix} 1 & x_1 & x_1^2 & x_1^3 \\ 0 & 1 & 2x_1 & 3x_1^2 \\ 0 & 0 & 2 & 6x_1 \\ 0 & 1 & 2x_2 & 3x_2^2 \end{pmatrix} \begin{pmatrix} a_0 \\ a_1 \\ a_2 \\ a_4 \end{pmatrix} = \begin{pmatrix} 0 \\ 0 \\ 0 \\ \arctan(\delta) \end{pmatrix}. \tag{11}$$

Several examples how the camber line of the airfoil can be modified using proposed method are shown in Figure 15. Vertical dashed lines correspond to the initial points of the morphing. Farfield topology was selected for this case. The influence of morphing start position is evaluated and compared against a conventional 20% aileron on LS0417 at low Reynolds number.

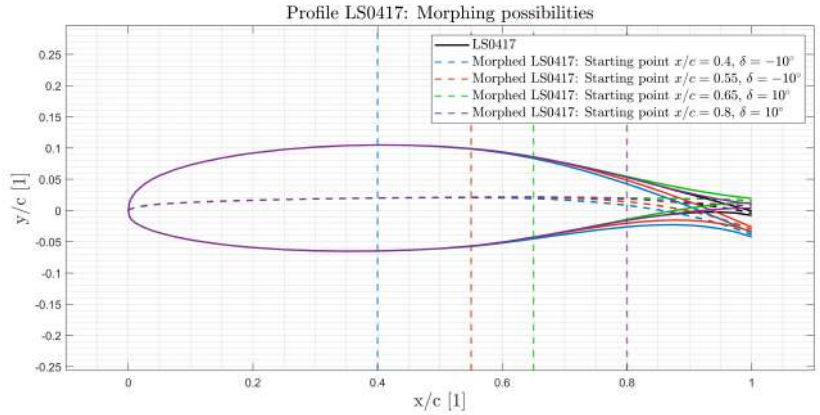


Figure 15 – LS0417: Morphing possibilities.

Efficiency curves of the morphed profiles are presented in Figure 16. The study shows that the beneficial effect is not restricted to a single geometry parameterization. In the reported comparison, there is a slight efficiency gain in case of $\delta = 10^\circ$ and in the case of $\delta = -10^\circ$, the peak efficiency gain of approximately 10% against standard aileron configuration is observed.

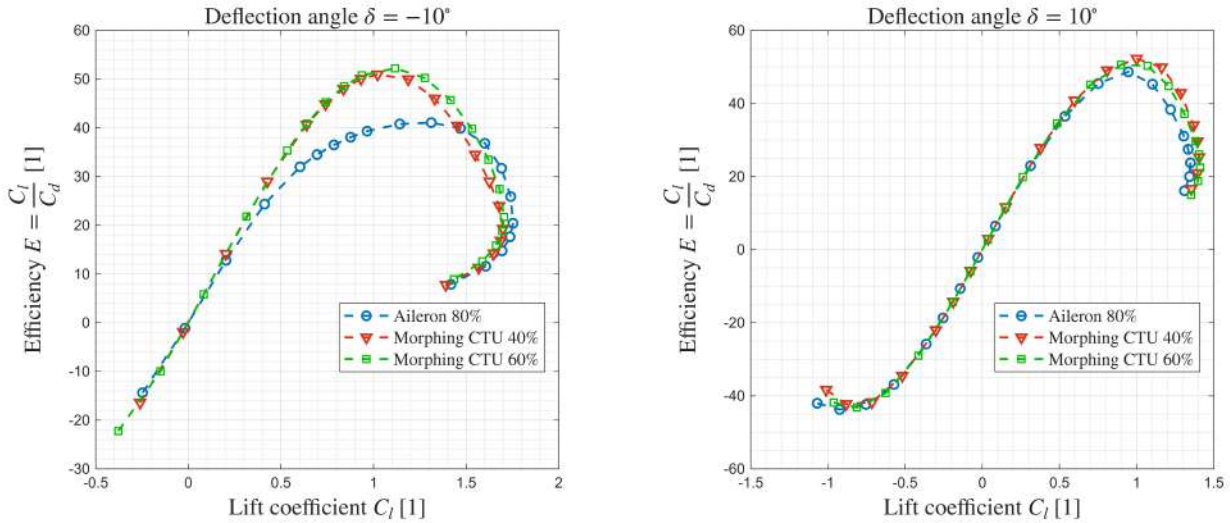


Figure 16 – LS0417 aileron configuration vs. morphing: Comparison of efficiency E of the morphed airfoil at Reynolds number $Re = 0.833 \times 10^6$ under deflection angles $\delta = \{-10, 10\}^\circ$.

Figure 17 compares pressure coefficient C_p distributions at zero angle of attack for the limit cases of proposed morphing methods, *i.e.*, $\delta = -10^\circ$ and $\delta = 10^\circ$ for the $\alpha = 0^\circ$. As it can be seen, the higher order continuity and smoothness of morphed airfoils resulted into a smooth course of the pressure coefficient distribution near the hinge position at 80% of the chord. Pressure distributions differ slightly when the trailing edge is morphed downwards by proposed method. In the opposite case, there are larger differences, but the bump near the hinge position is suppressed also.

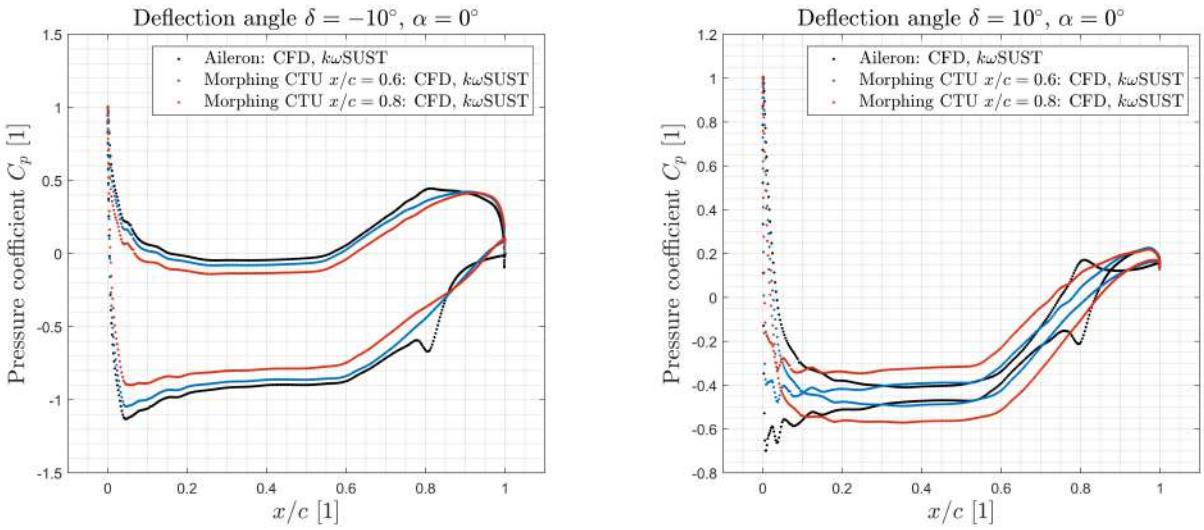


Figure 17 – LS0417 aileron configuration vs. morphing: Comparison of a pressure coefficient C_p distribution at Reynolds number $Re = 0.833 \times 10^6$ under deflection angles $\delta = \{-10, 10\}^\circ$ and zero angle of attack $\alpha = 0^\circ$.

3.2 Blockage effect in the wind tunnel

Next attempt is to examine influence of the blockage effect within the wind tunnel and differences that occur between measured model in the wind tunnel and real wing under freestream conditions. To simulate airfoil within the wind tunnel, mesh overset method was used as it is shown in Figure 18. Axis of the rotation is assumed as camber line coordinate at its quarter.

Case with the lowest possible aspect ratio, according to measurement space, is assumed, thus chord length was selected as $c = 250mm$, that corresponds to the tunnel height $h_{WT} = 2.8m$ in case of unitary airfoil chord. Since there is no need for the farfield correction, standard $k\omega$SST model with turbulence intensity $I = 0.1\%$ and turbulent viscosity to viscosity ratio $\nu_t/\nu = 0.1$ is employed.

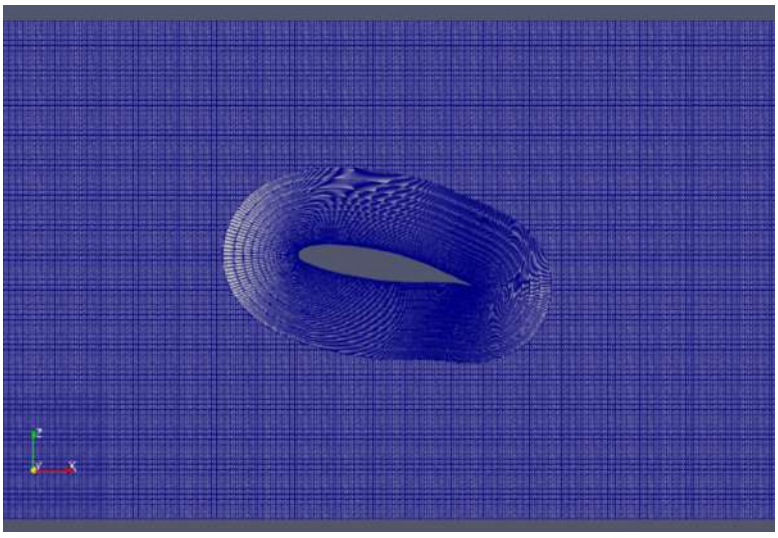


Figure 18 – Computational meshes overset.

The slope of the lift is different, that results into lower values at negative angles of attack and higher values at positive ones in comparison with freestream conditions as reports Figure 19. Influence of the wind tunnel walls appears to be significant in case of the pitching moment at the quarter of the chord $C_{m_{0.25c}}$. The slope of the curve is different at lower angles of attack, while at higher angles of attack, the slope seems to be similar, but the values are almost by 10% lower in case of the wind tunnel simulation.

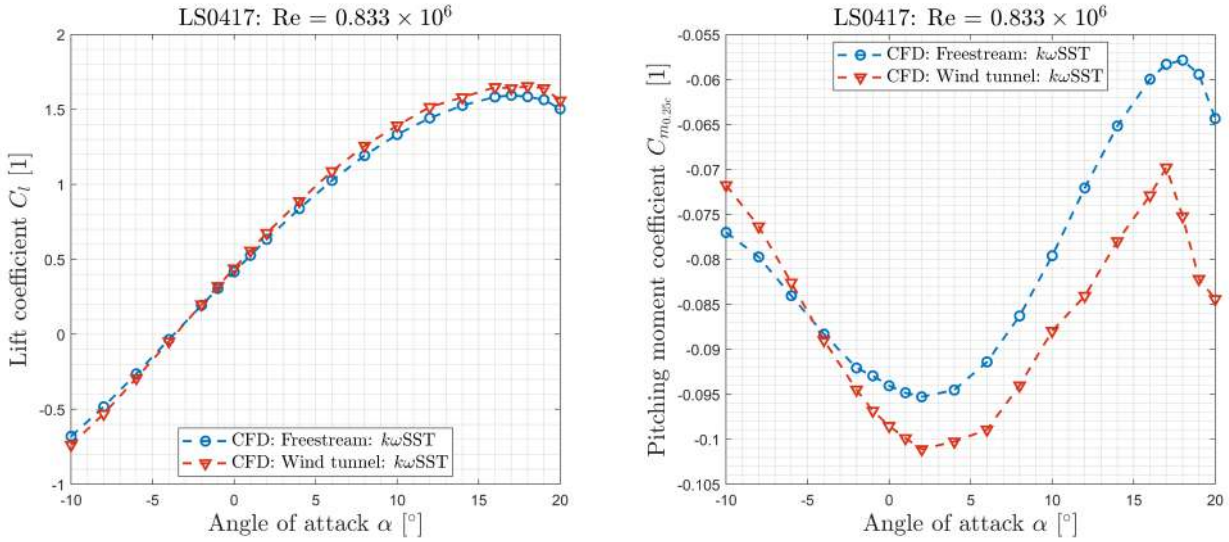


Figure 19 – LS0417 in a wind tunnel: Comparison of a lift coefficient C_l and drag coefficient C_d against angle of attack α at Reynolds number $Re = 0.833 \times 10^6$.

There are comparisons of the CFD results for the pressure coefficient distribution to investigate potential differences between freestream conditions and measurement within the wind tunnel. In the case higher angles of attack there is visible difference on the upper surface of the airfoil as shown in Figure 20. Pressure distributions on the lower surface of the profile differ slightly.

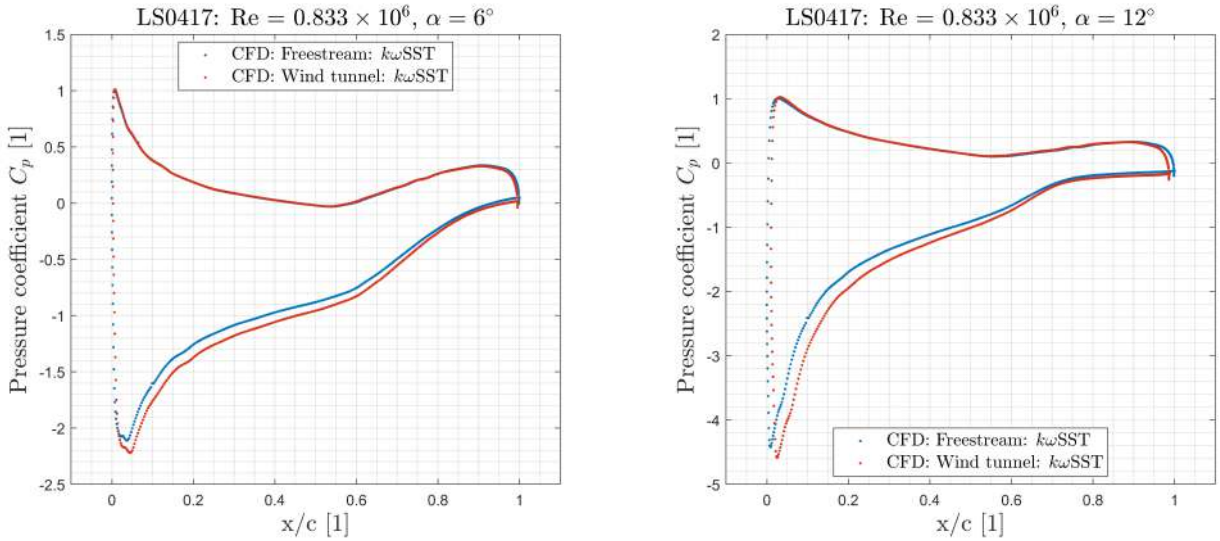


Figure 20 – LS0417 in a wind tunnel: Comparison of a pressure coefficient C_p distribution at Reynolds number $Re = 0.833 \times 10^6$ under angles of attack $\alpha = \{6, 12\}^\circ$.

Examination of the blockage effect and its influence to the overall aerodynamics parameters and pressure distributions was performed. It turned out that the difference between results obtained by simulation in the wind tunnel and under freestream conditions should not be neglected and should be taken into account when CFD simulations and experimental measurements are compared.

4. Conclusion

A validated incompressible CFD framework has been developed to assess morphing trailing edge aerodynamics under both freestream and wind tunnel conditions. Benchmark studies on NACA0012, LS0417, and FX66-S-196 V1 show that no single turbulence model is universally adequate; model selection must follow the physical flow regime. When this requirement is respected, continuous morphing trailing edges on LS0417 provide smoother loading, suppress hinge region pressure discontinuities, and improve peak aerodynamic efficiency relative to a conventional 20% aileron by approximately 10-15% in representative cases. Overall, the results support morphing trailing edges as a promising aerodynamic control surface concept and establish turbulence-model fidelity as a central requirement for their credible numerical assessment.

Importantly, the morphing related benefits identified in this work - smoother pressure distributions, improved efficiency, and reduced aerodynamic penalties - consistently emerge when turbulence and transition modeling reflects the underlying physical flow regime. This confirms that the observed advantages of morphing are robust aerodynamic features rather than numerical artifacts.

To support these findings, a fully parametrized and automated simulation framework was developed, enabling rapid reconfiguration of airfoil geometry, tunnel layout, angle of attack definition, and boundary conditions. The framework is directly applicable to future experimental campaigns and enhances consistency between numerical and measured results.

Overall, the work delivers a robust, validated, and extensible aerodynamic analysis methodology that combines high fidelity CFD, morphing wing aerodynamics, and wind-tunnel realism. The results strongly support the technical feasibility and aerodynamic benefits of morphing trailing edge concepts, while providing practical tools and insights for their continued development and experimental verification.

Future work should therefore include three-dimensional simulations of finite wings to capture spanwise effects, tip vortices, and structural aerodynamic interactions that cannot be resolved in a two-dimensional setting. Further work should also contain validation against dedicated wind tunnel experiments, particularly with time resolved measurements to assess unsteady effects and transition behavior. Finally, expanding the study to include optimization of morphing geometries and control strategies across a broader range of Reynolds numbers and operating conditions would provide deeper insight into performance gains and support the integration of morphing trailing edges into real world aerodynamic applications.

5. Contact Author Email Address

In case of any question or comment, please do not hesitate to contact the corresponding author on Patrik.Kovar@fs.cvut.cz.

6. Copyright Statement

The authors confirm that they, and/or their company or organization, hold copyright on all of the original material included in this paper. The authors also confirm that they have obtained permission, from the copyright holder of any third party material included in this paper, to publish it as part of their paper. The authors confirm that they give permission, or have obtained permission from the copyright holder of this paper, for the publication and distribution of this paper as part of the ICAS proceedings or as individual off-prints from the proceedings.

Acknowledgment

This work has received funding from the European Union's Horizon Europe research and innovation programme under grant agreement No 101159722, within the project "Twinning for excellence in morphing and aero-mechatronic wing control: A leap towards eco-smart aviation", funded under the call HORIZON-WIDERA-2023-ACCESS-02.

Funded by the European Union

TWING MECHA

References

[1] H. G. Weller, G. Tabor, H. Jasak, and Ch. Fureby. A tensorial approach to computational continuum mechanics using object-oriented techniques. *Computers in physics*, 12(6):620–631, 1998.

[2] S. Patankar. *Numerical heat transfer and fluid flow*. CRC press, 1980.

[3] N. Gregory and C. L. O'Reilly. Low-speed aerodynamic characteristics of naca 0012 aerofoil section, including the effects of upper-surface roughness simulating hoar frost. 1970.

[4] Ch. L. Ladson. *Effects of independent variation of Mach and Reynolds numbers on the low-speed aerodynamic characteristics of the NACA 0012 airfoil section*, volume 4074. National Aeronautics and Space Administration, 1988.

[5] P. Spalart and S. Allmaras. A one-equation turbulence model for aerodynamic flows. In *30th aerospace sciences meeting and exhibit*, page 439, 1992.

[6] S. L. Krist, R. T. Biedron, and Ch. L. Rumsey. Cfl3d user's manual (version 5.0). Technical report, 1998.

[7] R. J. McGhee and W. D. Beasley. *Low-speed aerodynamic characteristics of a 17-percent-thick airfoil section designed for general aviation applications*. National Aeronautics and Space Administration, 1973.

[8] R. J. McGhee. *Low-speed aerodynamic characteristics of a 17-percent-thick medium speed airfoil designed for general aviation applications*. National Aeronautics and Space Administration, 1980.

[9] F. R. Menter. Two-equation eddy-viscosity turbulence models for engineering applications. *AIAA journal*, 32(8):1598–1605, 1994.

[10] P. Spalart and Ch. L. Rumsey. Effective inflow conditions for turbulence models in aerodynamic calculations. *AIAA journal*, 45(10):2544–2553, 2007.

[11] R. J. McGhee and W. D. Beasley. Effects of thickness on the aerodynamic characteristics of an initial low-speed family of airfoils for general aviation applications. Technical report, 1976.

[12] R. J. McGhee, W. D. Beasley, and R. T. Whitcomb. Nasa low-and medium-speed airfoil development. In *NASA Conf. on Advanced Tech. Airfoil Res.*, number NASA-TM-78709, 1979.

[13] W. H. Wentz Jr, H. C. Seetharam, and K. A. Fiscko. Force and pressure tests of the ga (w)-1 airfoil with a 20% aileron and pressure tests with a 30% fowler flap. Technical report, NASA, 1977.

[14] F. X. Wortmann. A critical review of the physical aspects of airfoil design at low mach numbers. *NASA CR*, 2315:179–196, 1973.

[15] Inc. Ansys. Ansys cfx-solver theory guide. *Release 2021 R2*, 2021.

[16] F. R. Menter, P. E. Smirnov, T. Liu, and R. Avancha. A one-equation local correlation-based transition model. *Flow, Turbulence and Combustion*, 95:583–619, 2015.

[17] R. B. Langtry and F. R. Menter. Correlation-based transition modeling for unstructured parallelized computational fluid dynamics codes. *AIAA journal*, 47(12):2894–2906, 2009.

[18] F. R. Menter, R. B. Langtry, and S. Völker. Transition modelling for general purpose cfd codes. *Flow, turbulence and combustion*, 77:277–303, 2006.

[19] J. Gooden. Experimental low-speed aerodynamic characteristics of the wortmann fx 66-s-196 v1 airfoil. *Technical Soaring*, 5(3):21–31, 1979.